

## NMR Spectroscopy

How to cite: *Angew. Chem. Int. Ed.* **2020**, *59*, 11262–11266

International Edition: doi.org/10.1002/anie.202000493

German Edition: doi.org/10.1002/ange.202000493

# Extending the Sensitivity of CEST NMR Spectroscopy to Micro-to-Millisecond Dynamics in Nucleic Acids Using High-Power Radio-Frequency Fields

Atul Rangadurai, Honglue Shi, and Hashim M. Al-Hashimi\*

**Abstract:** Biomolecules undergo motions on the micro-to-millisecond timescale to adopt low-populated transient states that play important roles in folding, recognition, and catalysis. NMR techniques, such as Carr–Purcell–Meiboom–Gill (CPMG), chemical exchange saturation transfer (CEST), and  $R_{1\rho}$  are the most commonly used methods for characterizing such transitions at atomic resolution under solution conditions. CPMG and CEST are most effective at characterizing motions on the millisecond timescale. While some implementations of the  $R_{1\rho}$  experiment are more broadly sensitive to motions on the micro-to-millisecond timescale, they entail the use of selective irradiation schemes and inefficient 1D data acquisition methods. Herein, we show that high-power radio-frequency fields can be used in CEST experiments to extend the sensitivity to faster motions on the micro-to-millisecond timescale. Given the ease of implementing high-power fields in CEST, this should make it easier to characterize micro-to-millisecond dynamics in biomolecules.

Proteins and nucleic acids undergo structural dynamics over timescales ranging from picoseconds to seconds.<sup>[1]</sup> Motions on the micro-to-millisecond timescale frequently involve transitions from the energetically most favorable ground state (GS) conformation towards low-populated (typically less than 5%) and short-lived (lifetime less than 2 ms) excited conformational states (ESs) that typically have non-native conformations.<sup>[2]</sup> There has been great interest in characterizing such motions because they have been shown to play critical roles in folding<sup>[3]</sup> and function,<sup>[4]</sup> and because many ESs are attractive drug targets.<sup>[5]</sup> Different NMR experiments have been developed to characterize micro-to-millisecond timescale motions that rely on modulating the dephasing of magnetization due to chemical exchange by the application of radio-frequency (RF) fields.<sup>[6]</sup> Spin-relaxation in the rotating frame ( $R_{1\rho}$ )<sup>[7]</sup> is most effective at characterizing fast micro-second timescale motions while Carr–Purcell–Meiboom–Gill (CPMG)<sup>[8]</sup> and chemical exchange saturation transfer

(CEST)<sup>[9]</sup> are most effective at characterizing slower millisecond motions. Herein, we show that use of high-power RF fields extends the sensitivity of CEST to faster timescale motions. Given other established technical advantages of CEST,<sup>[10]</sup> this broadens the scope of characterizing micro-to-millisecond motions in biomolecules using NMR spectroscopy.

An exchange process is most effectively characterized when the effective field ( $\omega_{\text{eff}}$  in  $\text{rads}^{-1}$ ) experienced by a given nucleus is comparable to the rate of exchange ( $k_{\text{ex}} = k_1 + k_{-1}$ , where  $k_1$  and  $k_{-1}$  are the forward and backward rate constants, respectively).<sup>[11]</sup> Under these conditions, dephasing of magnetization due to chemical exchange is maximally modulated by the applied RF field. CPMG, CEST, and  $R_{1\rho}$  have different timescale sensitivities because they employ different schemes to apply the RF field, which in turn place different constraints on the range of  $\omega_{\text{eff}}$  values that can be attained.

CPMG employs a series of hard  $180^\circ$  pulses with varying time intervals to modulate dephasing of transverse magnetization.<sup>[12]</sup> The lower limit of  $\omega_{\text{eff}}/2\pi \approx 300$  Hz is determined by signal losses due to relaxation, while the upper limit of  $\omega_{\text{eff}}/2\pi \approx 12$  kHz is determined by the probe tolerance to high-power RF fields and sample heating.<sup>[10b,11]</sup> Thus, CPMG is typically sensitive to  $k_{\text{ex}}$  between about  $200 \text{ s}^{-1}$  and about  $4000 \text{ s}^{-1}$ .<sup>[12]</sup> Higher  $\omega_{\text{eff}}$  ( $\approx 100 \text{ Hz} < \omega_{\text{eff}}/2\pi < \approx 18 \text{ kHz}$ ) are accessible in the  $R_{1\rho}$  experiment, which employs spin-locking RF fields with variable power ( $\approx 100 \text{ Hz} < \omega_1/2\pi < \approx 5 \text{ kHz}$ ) and offset.<sup>[13]</sup> Therefore,  $R_{1\rho}$  is typically sensitive to a wider range of  $k_{\text{ex}}$  ( $\approx 400 \text{ s}^{-1} < k_{\text{ex}} < \approx 50000 \text{ s}^{-1}$ ) with the lower limit being determined by complications due to the evolution of homonuclear scalar couplings when using weak spin-locking fields,<sup>[10c]</sup> and the upper limit by the tolerance of the probe to high power RF fields.<sup>[14]</sup> Optimal sensitivity to slower exchange rates however typically necessitates the use of selective excitation for interrogating one spin at a time using 1D data acquisition schemes.<sup>[15]</sup> In contrast to  $R_{1\rho}$ , both CPMG and CEST are routinely performed in a 2D manner. CEST involves monitoring dephasing of longitudinal magnetization as a function of the applied RF-field strength and offset frequency.<sup>[10a,b,16]</sup> Weaker RF fields ( $\omega_1/2\pi < 100 \text{ Hz}$ ) relative to  $R_{1\rho}$  can also be used in CEST, making it more effective at characterizing slower exchange.<sup>[10a,17]</sup> CEST studies of biomolecules have typically used low-power RF fields ( $\omega_1/2\pi < 100 \text{ Hz}$ ) as higher powers lead to broadening of the dips in the CEST profiles, making it difficult to resolve distinct chemical shifts for the GS and ES.<sup>[16]</sup> This has limited the applicability of CEST to processes in the slow-exchange regime with  $k_{\text{ex}}$  between about  $20 \text{ s}^{-1}$  and about  $400 \text{ s}^{-1}$ .<sup>[10a]</sup>

[\*] A. Rangadurai, Prof. H. M. Al-Hashimi  
Department of Biochemistry, Duke University  
229, Nanaline Duke Building, 307 Research Drive, Durham, NC  
27710 (USA)  
E-mail: hashim.al.hashimi@duke.edu  
Homepage: <https://sites.duke.edu/alhashimilab/>

H. Shi, Prof. H. M. Al-Hashimi  
Department of Chemistry, Duke University  
Durham, NC 27708 (USA)

Supporting information and the ORCID identification number(s) for the author(s) of this article can be found under:  
<https://doi.org/10.1002/anie.202000493>.

Given the advantages of CEST relative to  $R_{1\rho}$ ,<sup>[10a]</sup> including its ease of implementation, we examined whether we could extend the sensitivity of CEST to faster timescale motions by employing higher power RF fields. In theory, there are no technical restrictions on using RF fields with powers as high as those used in  $R_{1\rho}$ .<sup>[18]</sup> Furthermore, studies have successfully extracted exchange parameters from CEST profiles of small-molecule systems in the intermediate–fast exchange regime using low-<sup>[19]</sup> and high-power<sup>[18a,b]</sup> RF fields, even though distinct dips for the GS and ES were not observed (Supporting Information, Discussion S1).

To test whether it is indeed feasible to characterize faster exchange processes using high-power CEST, we used the Bloch–McConnell (B–M) equations to simulate CEST and  $R_{1\rho}$  profiles for two-state GS↔ES exchange as a function of varying RF powers and  $k_{\text{ex}}$ . For small  $k_{\text{ex}}$  ( $300 \text{ s}^{-1}$ ,  $\tau_{\text{ex}} = 1/k_{\text{ex}} = 3.3 \text{ ms}$ ) in the slow-exchange regime ( $k_{\text{ex}}/\Delta\omega < 1$ ), conventional low power CEST profiles displayed the characteristic dip at an offset corresponding to the ES chemical shift ( $\omega_{\text{ES}}$ , Figure 1). As  $k_{\text{ex}}$  was increased to the intermediate ( $k_{\text{ex}} = 3,000 \text{ s}^{-1}$ ,  $\tau_{\text{ex}} = 0.33 \text{ ms}$ ,  $k_{\text{ex}}/\Delta\omega \approx 1$ ) and fast ( $k_{\text{ex}} = 9,000 \text{ s}^{-1}$ ,  $\tau_{\text{ex}} = 0.11 \text{ ms}$ ,  $k_{\text{ex}}/\Delta\omega > 1$ ) exchange regimes, the ES dip gradually broadened and diminished in size, and the profiles became increasingly insensitive to the exchange process, showing little deviations from the profiles simulated in the absence of exchange (Figure 1, solid vs. dashed lines).<sup>[10a]</sup> This highlights the challenge of characterizing faster processes using low-power CEST. As expected, for small  $k_{\text{ex}}$  in the slow-exchange regime, the ES dip was broadened out to a shoulder

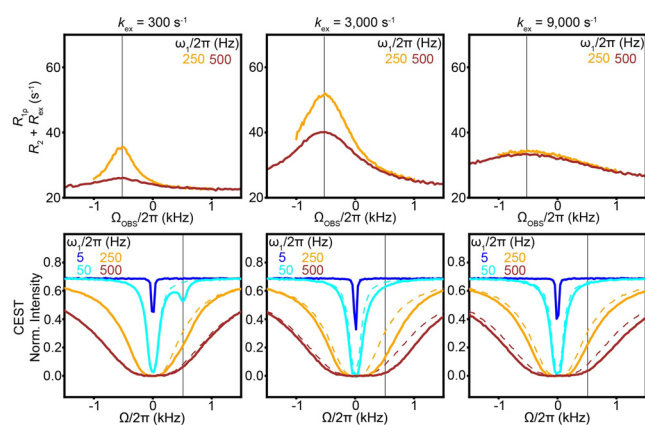


**Figure 1.** Simulated off-resonance  $R_{1\rho}$  and CEST profiles (solid lines) for varying  $k_{\text{ex}}$  and RF powers (color-coded). Simulated CEST profiles in the absence of exchange are shown as dashed lines.  $\Omega_{\text{OBS}} = \omega_{\text{OBS}} - \omega_{\text{RF}}$  and  $\Omega = \omega_{\text{RF}} - \omega_{\text{OBS}}$ , where  $\omega_{\text{OBS}}$  is the Larmor frequency of the observed resonance and  $\omega_{\text{RF}}$  is the angular frequency of the RF field. Vertical black line corresponds to  $\Omega = \omega_{\text{ES}}$ . Simulations assumed  $\Delta\omega(^{13}\text{C}) = 3.0 \text{ ppm}$ ,  $\gamma(^1\text{H})B_0/2\pi = 700 \text{ MHz}$ ,  $R_{1,\text{GS}} = R_{1,\text{ES}} = 2.5 \text{ s}^{-1}$ , and  $R_{2,\text{GS}} = R_{2,\text{ES}} = 22.5 \text{ s}^{-1}$ . Relaxation delays of 0.15 s and 0.25 s were used for the CEST and  $R_{1\rho}$  simulations, respectively. An RF field inhomogeneity of 3% was used for the CEST simulations as described in the Materials and Methods in the Supporting Information. Complete equilibration of magnetization prior to the relaxation delay was assumed for both simulations. Alignment of magnetization for the  $R_{1\rho}$  simulations was performed as described previously.<sup>[13]</sup> Error was applied to the simulated profiles as described in the Materials and Methods in the Supporting Information.

with increasing RF powers that was more pronounced for offsets in the direction of  $\omega_{\text{ES}}$  relative to offsets in the direction opposite to  $\omega_{\text{ES}}$ . This behavior is analogous to that seen routinely in off-resonance  $R_{1\rho}$ .<sup>[20]</sup> Interestingly, the shoulder in the high-power CEST profiles persisted even for large  $k_{\text{ex}}$  values in the intermediate- and fast-exchange regimes, when the low-power CEST profiles were increasingly insensitive to the exchange (Figure 1). Furthermore, the size of the shoulder qualitatively mirrored the magnitude of  $R_{\text{ex}}$  in the high spin-lock  $R_{1\rho}$  profiles. Further simulations showed that the high-power CEST profiles could be fit to the B–M equations to accurately extract the exchange parameters (Supporting Information, Figure S1). This indicates that using high-power RF fields in CEST could broaden the accessible window to faster exchange rates.

We tested the feasibility of using high-power CEST to characterize two exchange processes on the slow-to-intermediate exchange timescale with  $k_{\text{ex}} \approx 3000 \text{ s}^{-1}$ . We first examined exchange between wobble G–T mismatches and their Watson–Crick-like counterparts formed by tautomerization of the bases (Figure 2A). This exchange process was previously characterized using off-resonance  $R_{1\rho}$  experiments<sup>[21]</sup> targeting the base imino nitrogen (G–N1, T–N3) and carbon (T–C6) nuclei (Figure 2B and Supporting Information, Tables S1 and S2, and Discussion S2). The magnitude of  $k_{\text{ex}} = 2689 \pm 163 \text{ s}^{-1}$  exceeds the typical detection limit of about  $400 \text{ s}^{-1}$  for low-power CEST.<sup>[10a]</sup> Consequently, as expected, low-power CEST profiles for these nuclei did not show ES dips and exhibited minor deviations from simulated profiles in the absence of exchange (Figure 2B, dashed lines). Moreover, fitting of the profiles did not yield reliable exchange parameters (Supporting Information, Figures S2 and S3, and Tables S1, S2, and S4). In contrast, as predicted from B–M simulations (Figure 1), the high-power CEST profiles exhibited ES dips (G15–N1 and T5–N3, owing to a large  $\Delta\omega$ ) or a broad shoulder (T5–C6, owing to a smaller  $\Delta\omega$ , Figure 2B). This shoulder is best visualized when comparing the normalized intensity for a given positive value of the offset  $\Omega_i$  relative to its corresponding negative counterpart  $-\Omega_i$  (Figure 2C), in which intensities are smaller for offsets in the direction of  $\omega_{\text{ES}}$ . Fitting of the high-power CEST profiles was significantly improved with the inclusion of conformational exchange and RF-field inhomogeneity (Supporting Information, Figures S4–S6, Table S3, and Materials and Methods), which was essential to obtain accurate estimates of the exchange parameters. Furthermore, the influence of homonuclear  $^{13}\text{C}$ – $^{13}\text{C}$  scalar couplings ( $^1J_{\text{C5-C6}} \approx 67 \text{ Hz}$ ) when fitting the CEST data for T5–C6 was considered only for the low-RF-power profiles for which  $\omega_1/2\pi < ^1J_{\text{C-C}}$ , as they are suppressed when using high RF powers for which  $\omega_1/2\pi > ^1J_{\text{C-C}}$ <sup>[10a]</sup> (Supporting Information, Materials and Methods). The profiles for G15–N1, T5–N3, and T5–C6 could be globally fitted to yield ES population  $p_{\text{B}} = 0.180 \pm 0.001 \%$ ,  $k_{\text{ex}} = 3025 \pm 19 \text{ s}^{-1}$  ( $\tau_{\text{ex}} = 0.33 \text{ ms}$ ) and chemical shift differences between the ES and GS ( $\Delta\omega = \omega_{\text{ES}} - \omega_{\text{GS}}$ ) that were in excellent agreement with those obtained using  $R_{1\rho}$  (Figure 2D, and Supporting Information, Figure S3, Tables S1, S2, and S4, and Discussions S2 and S3). Furthermore, as negative controls, nuclei with flat  $R_{1\rho}$  profiles with no

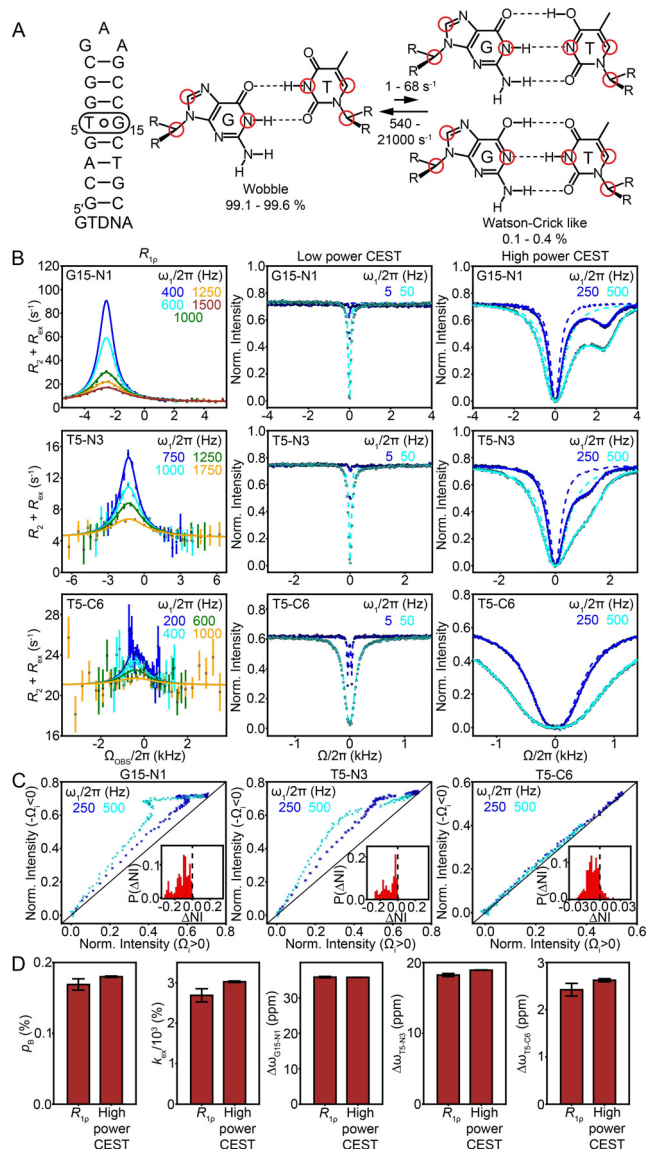


**Figure 2.** A) The GTDNA DNA hairpin (left) and the exchange between the wobble and Watson–Crick-like G–T mismatches (right). Exchange parameters were obtained as described previously.<sup>[4a]</sup> Probes used to measure  $R_{1p}$  and CEST are highlighted in circles. B) Comparison of off-resonance  $R_{1p}$  (left) with low (middle) and high (right) power CEST profiles. A two-state global fit of the data for G15-N1, T5-N3, and T5-C6 to the B–M equations is shown as solid lines. The relaxation rate constants  $R_1$  and  $R_2$  for the CEST simulations with no exchange (dashed lines) were obtained from the global fits. RF field inhomogeneity was taken into account during CEST fitting and simulation as described in the Materials and Methods in the Supporting Information. Alignment of magnetization for  $R_{1p}$  fitting was performed as described previously.<sup>[13]</sup> C) Correlation plots of the normalized intensity (NI) for positive ( $\Omega_i > 0$ ) and negative ( $-\Omega_i < 0$ ) offsets of the high-power CEST profiles, where  $\Omega_i$  is the  $i^{\text{th}}$  positive offset value. Solid line denotes a straight line with unit slope. Inset: Histogram of  $\Delta\text{NI} = \text{NI}(\Omega_i > 0) - \text{NI}(-\Omega_i < 0)$ . Dashed line denotes identical normalized intensities for positive and corresponding negative offsets. D) Comparison of exchange parameters obtained from global fitting of  $R_{1p}$  and high-power CEST profiles. RF powers for  $R_{1p}$  and CEST are color-coded. Error bars for the CEST intensities and exchange parameters were obtained as described in the Materials and Methods in the Supporting Information, while error bars in the  $R_{1p}$  profiles were obtained as described previously.<sup>[13]</sup> Error bars for the CEST intensities are smaller than the data points.

dispersion (G15-C1' and T5-C1') (Figure 3) also showed no signs of chemical exchange in high-power CEST. The normalized intensities for positive and negative offsets for these nuclei were similar to each other (Figure 3), and their profiles showed no visual improvement in fit quality on inclusion of exchange (Supporting Information, Figure S7).

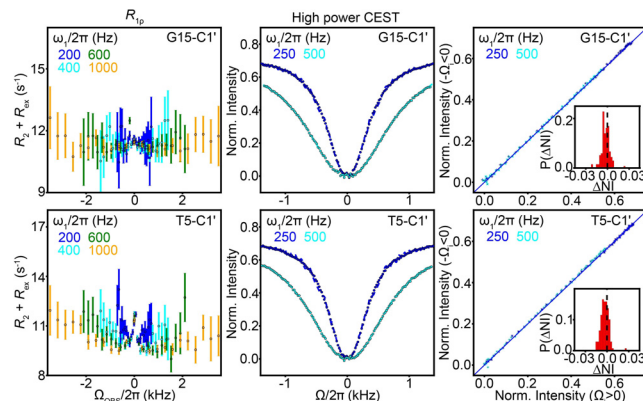


**Figure 3.** Off-resonance  $R_{1p}$  (left) and high-power CEST profiles (middle) for G15-C1' and T5-C1' in GTDNA. Relaxation rate constants  $R_1$  and  $R_2$  for the CEST simulations with no exchange (dashed lines) were obtained from individual fits of the high-power CEST data. RF field inhomogeneity was taken into account for the CEST simulation and fitting as described in the Materials and Methods in the Supporting Information. Right: Correlation plots of the normalized intensity (NI) for positive ( $\Omega_i > 0$ ) and negative ( $-\Omega_i < 0$ ) offsets of the high-power CEST profiles, where  $\Omega_i$  is the  $i^{\text{th}}$  positive offset value. Solid line denotes a straight line with unit slope. Inset: Histogram of  $\Delta\text{NI} = \text{NI}(\Omega_i > 0) - \text{NI}(-\Omega_i < 0)$ . Dashed line denotes identical normalized intensities for positive and corresponding negative offsets. RF powers for  $R_{1p}$  and CEST are color-coded. Error bars for the  $R_{1p}$  profiles and CEST intensities were obtained as described previously,<sup>[13]</sup> and in the Materials and Methods in the Supporting Information, respectively. Error bars for the CEST intensities are smaller than the data points.

As a second test, we used high-power CEST to characterize the exchange between A–T Watson–Crick and Hoogsteen base pairs that are formed by flipping the adenine base about the glycosidic bond. These experiments were performed on a uniformly  $^{13}\text{C}/^{15}\text{N}$ -labelled DNA duplex (A<sub>6</sub>-DNA, Figure 4A). Based on  $R_{1p}$ , this process can be characterized using the A-C8 and sugar A-C1' nuclei (Figure 4B and Supporting Information, Table S5). As expected given the large  $k_{\text{ex}} = 3775 \pm 163 \text{ s}^{-1}$ , low-power CEST profiles for these nuclei did not display ES dips, showed minor deviations from simulated profiles in the absence of exchange (Figure 4B, dashed lines), and did not yield reliable exchange parameters on fitting (Supporting Information, Figures S3 and S8, and Table S5). Furthermore, the exchange was more effectively characterized using high-power RF fields, which yielded CEST profiles for A16-C1' and A16-C8 with broad shoulders (Figures 4B,C) that could be globally fitted to yield  $p_{\text{B}} = 0.316 \pm 0.009\%$ ,  $k_{\text{ex}} = 3585 \pm 70 \text{ s}^{-1}$  ( $\tau_{\text{ex}} = 0.28 \text{ ms}$ ), and ES  $\Delta\omega$  values that were in excellent agreement with those determined using  $R_{1p}$  (Figure 4D and Supporting Information, Figure S3, Table S5, and Discussion S3). Again, nuclei with flat  $R_{1p}$  profiles with no dispersion (A16-C2, T9-C6, and T9-C1') did

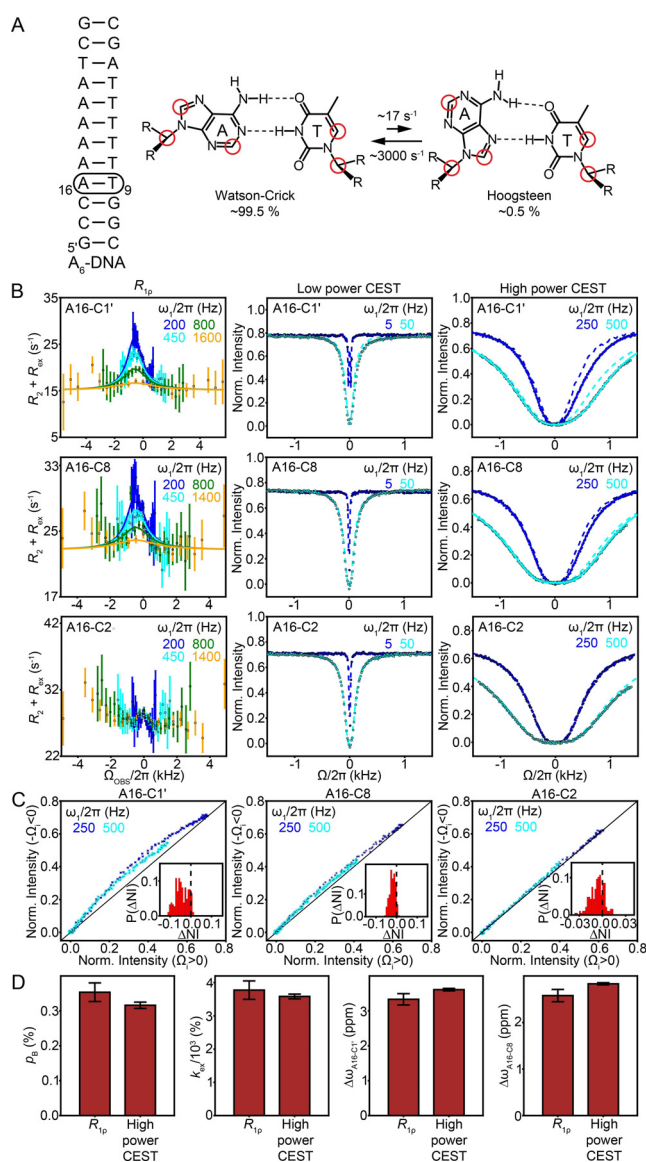


**Figure 4.** A) The A<sub>6</sub>-DNA duplex (left) and exchange between Watson-Crick and Hoogsteen A-T base pairs (right). Exchange parameters were obtained as described previously.<sup>[22]</sup> Probes used to measure  $R_{1\rho}$  and CEST are highlighted as red circles. B) Comparison of off-resonance  $R_{1\rho}$  (left) with low (middle) and high (right) power CEST profiles. A two-state global fit of the data for A16-C1' and A16-C8 to the B-M equations is shown as solid lines. The relaxation rate constants  $R_1$  and  $R_2$  for the CEST simulations with no exchange (dashed lines) for A16-C1' and A16-C8 were obtained from a global fit of their high-power CEST data, while those for A16-C2 were obtained from an individual fit of its high-power CEST data. RF field inhomogeneity for the CEST simulation and fitting was taken into account as described in the Materials and Methods in the Supporting Information. Alignment of magnetization for  $R_{1\rho}$  fitting was performed as described previously.<sup>[13]</sup> C) Correlation plots of the normalized intensity (NI) for positive ( $\Omega_i > 0$ ) and negative ( $-\Omega_i < 0$ ) offsets of the high-power CEST profiles, where  $\Omega_i$  is the  $i^{\text{th}}$  positive offset value. Solid line denotes a straight line with unit slope. Inset: Histogram of  $\Delta NI = NI(\Omega_i > 0) - NI(-\Omega_i < 0)$ . Dashed line denotes identical intensities for positive and corresponding negative offsets. D) Comparison of exchange parameters obtained from global fitting  $R_{1\rho}$  and high-power CEST profiles. RF powers for  $R_{1\rho}$  and CEST are color-coded. Error bars for the exchange parameters and CEST intensities were obtained as described in the Materials and Methods in the Supporting Information, while error bars in the  $R_{1\rho}$  profiles were obtained as described previously.<sup>[13]</sup> Error bars for the CEST intensities are smaller than the data points.

## Acknowledgements

We would like to thank Dr. Hala Abou Assi and Bei Liu for providing the samples used in the RF field inhomogeneity measurements. The research in this article was funded by US National Institutes of Health Grants R01GM089846 and R01GM132899 to Hashim M. Al-Hashimi.

## Conflict of interest

The authors declare no conflict of interest.

**Keywords:** biophysics · chemical exchange saturation transfer · DNA structures · nucleic acids · structural dynamics

not show detectable exchange in high-power CEST experiments (Figures 4B,C and Supporting Information, Figure S9).

In conclusion, high-power RF fields extend the window of exchange timescales accessible to CEST, from milliseconds in the slow-exchange regime, to micro-to-milliseconds in the intermediate- and fast-exchange regimes (Supporting Information, Discussion S4). By aligning the magnetization of all nucleic along  $z$ , CEST effectively overcomes limitations related to aligning magnetization of many nuclei that have limited the applicability of 2D  $R_{1\rho}$  experiments.<sup>[23]</sup> By making it easier to characterize biomolecular dynamics on the micro-to-millisecond timescale, we anticipate that the approach outlined in this study will facilitate the characterization of ESs in nucleic acids and proteins.

- [1] a) A. M. Mustoe, C. L. Brooks, H. M. Al-Hashimi, *Annu. Rev. Biochem.* **2014**, *83*, 441–466; b) A. K. Mittermaier, L. E. Kay, *Trends Biochem. Sci.* **2009**, *34*, 601–611.
- [2] a) A. Sekhar, L. E. Kay, *Proc. Natl. Acad. Sci. USA* **2013**, *110*, 12867–12874; b) B. Zhao, Q. Zhang, *Curr. Opin. Struct. Biol.* **2015**, *30*, 134–146.
- [3] a) Y. Xue, B. Gracia, D. Herschlag, R. Russell, H. M. Al-Hashimi, *Nat. Commun.* **2016**, *7*, 0; b) D. M. Korzhnev, X. Salvatella, M. Vendruscolo, A. A. Di Nardo, A. R. Davidson, C. M. Dobson, L. E. Kay, *Nature* **2004**, *430*, 586–590.
- [4] a) I. J. Kimsey, E. S. Szymanski, W. J. Zahurancik, A. Shakya, Y. Xue, C. C. Chu, B. Sathyamoorthy, Z. Suo, H. M. Al-Hashimi, *Nature* **2018**, *554*, 195–201; b) M. Wolf-Watz, V. Thai, K. Henzler-Wildman, G. Hadjipavlou, E. Z. Eisenmesser, D. Kern, *Nat. Struct. Mol. Biol.* **2004**, *11*, 945–949.
- [5] L. R. Ganser, C. C. Chu, H. P. Bogerd, M. L. Kelly, B. R. Cullen, H. Al-Hashimi, *Cell Rep.* **2020**, *30*, 2472–2480.e4.
- [6] A. G. Palmer III, *J. Magn. Reson.* **2014**, *241*, 3–17.

- [7] I. Solomon, *C. R. Hebd. Seances Acad. Sci.* **1959**, *249*, 1631–1632.
- [8] a) H. Y. Carr, E. M. Purcell, *Phys. Rev.* **1954**, *94*, 630–638; b) S. Meiboom, D. Gill, *Rev. Sci. Instrum.* **1958**, *29*, 688–691.
- [9] S. Forsén, R. Hoffman, *J. Chem. Phys.* **1963**, *39*, 2892–2901.
- [10] a) P. Vallurupalli, A. Sekhar, T. Yuwen, L. E. Kay, *J. Biomol. NMR* **2017**, *67*, 243–271; b) P. Vallurupalli, G. Bouvignies, L. E. Kay, *J. Am. Chem. Soc.* **2012**, *134*, 8148–8161; c) B. Zhao, A. L. Hansen, Q. Zhang, *J. Am. Chem. Soc.* **2014**, *136*, 20–23.
- [11] A. G. Palmer III, C. D. Kroenke, J. P. Loria, *Methods Enzymol.* **2001**, *339*, 204–238.
- [12] D. M. Korzhnev, L. E. Kay, *Acc. Chem. Res.* **2008**, *41*, 442–451.
- [13] A. Rangadurai, E. S. Szymaski, I. J. Kimsey, H. Shi, H. M. Al-Hashimi, *Prog. Nucl. Magn. Reson. Spectrosc.* **2019**, *112–113*, 55–102.
- [14] D. Ban, A. D. Gossert, K. Giller, S. Becker, C. Griesinger, D. Lee, *J. Magn. Reson.* **2012**, *221*, 1–4.
- [15] D. M. Korzhnev, V. Y. Orekhov, L. E. Kay, *J. Am. Chem. Soc.* **2005**, *127*, 713–721.
- [16] N. J. Anthis, G. M. Clore, *Q. Rev. Biophys.* **2015**, *48*, 35–116.
- [17] H. Shi, B. Liu, F. Nussbaumer, A. Rangadurai, C. Kreutz, H. M. Al-Hashimi, *J. Am. Chem. Soc.* **2019**, *141*, 19988–19993.
- [18] a) V. Khlebnikov, W. J. M. van der Kemp, H. Hoogduin, D. W. J. Klomp, J. J. Prompers, *Sci. Rep.* **2019**, *9*, 1089; b) M. Zaiss, A. Anemone, S. Goerke, D. L. Longo, K. Herz, R. Pohmann, S. Aime, M. Rivlin, G. Navon, X. Golay, K. Scheffler, *NMR Biomed.* **2019**, *32*, e4113; c) M. Zaiss, G. Angelovski, E. Demetriou, M. T. McMahon, X. Golay, K. Scheffler, *Magn. Reson. Med.* **2018**, *79*, 1708–1721.
- [19] a) V. Ramanujam, C. Charlier, A. Bax, *Angew. Chem. Int. Ed.* **2019**, *58*, 15309–15312; *Angew. Chem.* **2019**, *131*, 15453–15456; b) L. Avram, A. D. Wishard, B. C. Gibb, A. Bar-Shir, *Angew. Chem. Int. Ed.* **2017**, *56*, 15314–15318; *Angew. Chem.* **2017**, *129*, 15516–15520.
- [20] O. Trott, D. Abergel, A. G. Palmer III, *Mol. Phys.* **2003**, *101*, 753–763.
- [21] I. J. Kimsey, K. Petzold, B. Sathyamoorthy, Z. W. Stein, H. M. Al-Hashimi, *Nature* **2015**, *519*, 315–320.
- [22] H. S. Alvey, F. L. Gottardo, E. N. Nikolova, H. M. Al-Hashimi, *Nat. Commun.* **2014**, *5*, 4786.
- [23] F. Massi, E. Johnson, C. Wang, M. Rance, A. G. Palmer III, *J. Am. Chem. Soc.* **2004**, *126*, 2247–2256.

Manuscript received: January 10, 2020

Revised manuscript received: March 7, 2020

Accepted manuscript online: March 13, 2020

Version of record online: May 11, 2020